Anomalous quantum interference effects in graphene SNS junctions due to strain-induced gauge fields

Hadi Khanjani[1] and Ali G. Moghaddam[1,2,*]

[1]*Department of Physics, Institute for Advanced Studies in Basic Sciences (IASBS), Zanjan 45137-66731, Iran*
[2]*Research Center for Basic Sciences & Modern Technologies (RBST), Institute for Advanced Studies in Basic Science (IASBS), Zanjan 45137-66731, Iran*

We investigate the influence of gauge fields induced by strain on the supercurrent passing through the graphene-based Josephson junctions. We show that, in the presence of a constant pseudomagnetic field $\mathbf{B}_S$ originating from an arc-shape elastic deformation, the Josephson current is monotonically enhanced. This is in contrast with the oscillatory behavior of supercurrent (known as Fraunhofer pattern) caused by real magnetic fields passing through the junction. The absence of oscillatory supercurrent originates from the fact that strain-induced gauge fields have opposite directions at the two valleys due to the time-reversal symmetry. Subsequently the Aharonov-Bohm phases due to $\mathbf{B}_S$ cancel out between electron and hole components of the current carrying Andreev bound states. Nevertheless, we find another phase factor coming from the pseudomagnetic fields which rotates the pseudospin and is in fact responsible for the enhancement of Josephson currents. When both magnetic and pseudomagnetic fields are present, Fraunhofer-like oscillations as a function of the real magnetic field flux are found. Intriguingly, the combination of two kinds of gauge fields results in two special fingerprints in the local supercurrent density: (i) strong localization of the Josephson current density with more intense maximum amplitudes; (ii) appearance of the inflated vortex cores—finite regions with almost diminishing Josephson currents—whose sizes increase by increasing $\mathbf{B}_S$. These findings reveal unexpected interference signatures of pseudomagnetic fields in graphene SNS junctions which can cause a twist in the investigations on strain-induced gauge fields.

I. INTRODUCTION

Synthesis of graphene as the leading material among two-dimensional (2D) atomic monolayer has opened a new era in condensed-matter physics by putting forward many fundamental questions besides different applications [1,2]. One of the groundbreaking findings is about the appearance of gauge fields originating from elastic deformations [3–8]. These gauge fields originate from the relativistic spectrum of graphene and the fact that the main effect of smooth strain is to relocate and deform the Dirac cones in the corners of the Brillouin zone [8]. Subsequently, the dynamics of electrons in strained graphene is reminiscent of motion at the presence of a magnetic vector potential $\mathbf{A}$ but with a special property of having opposite signs at the two Dirac points, to preserve time-reversal symmetry (TRS) [9,10]. The existence of such pseudomagnetic fields has been experimentally validated by some experiments, especially using spectroscopy of Landau level at the vicinity of a highly strained nanobubble which has shown very large fields exceeding a few hundred T [11].

While many theoretical and experimental investigations have been carried out to understand and exploit the strain-induced gauge fields for possible applications, only a few works focused on the interference phenomena, especially the Aharonov-Bohm effect due to the gauge fields [12].

Historically, most of the quantum interference phenomena observed in solid-state systems have been associated with superconductors (S) because of the robust phase coherence of Cooper pairs [13–20]. Of particular interest, when a magnetic flux Φ_B is imposed to the nonsuperconducting or normal (N) region sandwiched between two superconductors, the critical supercurrent I_c shows a diffraction pattern by varying Φ_B. In addition, the local current density inside the N region reveals the so-called Josephson vortices which are governed by quantum-mechanical interferences in contrast to the Abrikosov vortex lattice where electrostatics plays a major physical role [21–23]. Putting all these together, we come up with the idea that superconductor-graphene-superconductor (SGS) junctions are very promising for exploring quantum interference phenomena due to the strain-induced gauge fields in graphene.

Over the last decade, many theoretical works have been focused on SGS and other graphene based superconducting heterostructures and found various peculiar and unexpected behaviors [24–32]. Most of the these features originate from Dirac dispersion of quasiparticles as well as the 2D nature of graphene as pointed out by Beenakker [24,30]. Interestingly, various experiments have even outpaced theory due to the impressive techniques in fabrication of high quality graphene based devices and very good contacts with various superconducting materials [33–46]. Some recent works have studied exhaustively the Fraunhofer pattern in SGS junctions [42,43,47]. In addition, a few works have investigated the

*agorbanz@iasbs.ac.ir

interplay of superconductivity with gauge fields at very high strain regimes in which pseudo-Landau levels are formed [48–50]. It has been found that when the pseudo-Landau levels are partially filled a superconducting state originating from electron-phonon coupling can survive at the weak-coupling limit [48]. On the other hand, Josephson current through graphene at the presence of high strains is strongly suppressed in long junctions [50]. Nevertheless, the effect of weak gauge fields and particularly the corresponding quantum interferences in the SGS systems have remained unexplored so far.

Here, based on a semiclassical framework, we show under a general gauge potential $\mathcal{A}$ that two different phases χ and χ' are gained by the quasiparticles' wave functions. The first phase χ depends on the flux of gauge field resembling the well-known Aharonov-Bohm (AB) effect, while χ' acting as a relative phase between the two components of the Dirac spinor depends on the circumference of the quasiparticles' trajectories. As a key finding, it is demonstrated that the Josephson current is enhanced at the presence of a uniform strain-induced pseudomagnetic field $\mathbf{B}_S$. In fact, an oscillatory Fraunhofer-like pattern of supercurrent is absent since the strain-induced AB phases gained by the electron and hole making a bound state cancel each other. Nevertheless, when a real magnetic field $\mathbf{B}$ is imposed to the junction beside the pseudomagnetic field, the Fraunhofer pattern is established by its variation. Further investigation of the combined effect of real and strain-induced fields reveals that Josephson vortices are strongly influenced by the presence of $\mathbf{B}_S$. In one hand, the gauge field's presence further localizes the vortex pattern. On the other hand, new vortex cores appear and inflate significantly at the presence of gauge fields which means finite regions of almost vanishing supercurrent emerge, having very sharp boundaries with nonvanishing supercurrent regions.

The paper is organized as follows. After the Introduction, in Sec. II the basic model, semiclassical framework for the calculations, and the main relations for the supercurrent are presented. Then, in Sec. III the Josephson current and its local density dependence on the gauge fields are shown followed by a discussion over the importance of the results and their experimental relevance. Finally, Sec. IV is devoted to the concluding remarks.

II. MODEL AND BASIC FORMALISM

Our model consists of an SGS junction where two superconducting electrodes are deposited over graphene with distance L from each other as depicted in Fig. 1(a). The normal graphene region is imposed to an arc-shaped strain or alternatively deformation with triangular symmetry which can lead to a uniform pseudomagnetic field $\mathbf{B}_S = B_S \mathbf{z}$ acting on the Dirac quasiparticles [9,10]. The strain-induced field and corresponding gauge potential $\mathbf{A}_S$ ($\nabla \times \mathbf{A}_S \equiv \mathbf{B}_S$) have opposite signs at the vicinity of the two Dirac points K and K' at the corners of hexagonal first Brillouin zone [8]. The underlying deep reason for the sign change originates from the facts that strain and any geometric deformation do not break TRS, and the two K points or valleys are connected by time-reversal operator ($K \overset{\Theta}{\longleftrightarrow} K'$). Putting together the low-energy Hamiltonian of normal graphene around Dirac points and at
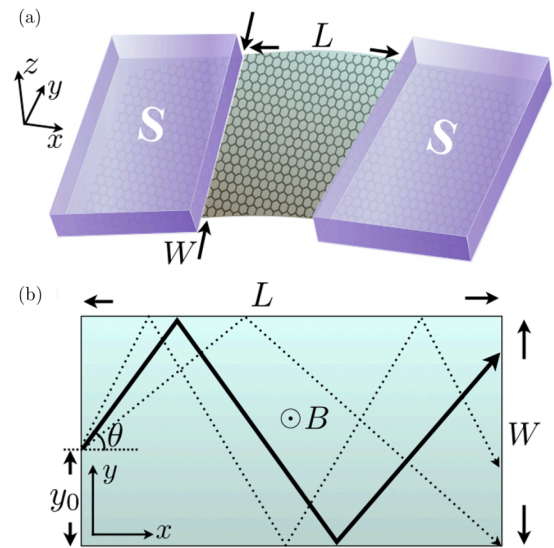

FIG. 1. (a) Schematic of the SGS Josephson junction with strained graphene at the middle. (b) The classical trajectories of Dirac excitations inside the normal graphene. The gauge fields are weak enough so that they cannot deflect the trajectories and only phase effects corresponding to them can come into play. The geometric parametrization of the trajectories and the normal region are shown.

the presence of both strain-induced gauge potentials and real magnetic fields ($\mathbf{B} = \nabla \times \mathbf{A}$) can be written as

$$\check{\mathcal{H}}(\mathbf{A}, \mathbf{A_S}) = v_F \begin{pmatrix} \hat{\boldsymbol{\sigma}} \cdot \boldsymbol{\Pi}_K & 0 \\ 0 & \hat{\boldsymbol{\sigma}}^* \cdot \boldsymbol{\Pi}_{K'} \end{pmatrix}, \qquad (1)$$

with $\boldsymbol{\Pi}_{K,K'} = \mathbf{p} + e(\mathbf{A} \pm \mathbf{A}_S)$ indicating the kinematical momenta at the vicinity of two valleys and $\hat{\boldsymbol{\sigma}} = (\sigma_x, \sigma_y)$ the Pauli matrices in the sublattice or pseudospin space. Here the Fermi velocity is denoted by v_F and $\mathbf{p} = (p_x, p_y)$ is the 2D momentum. Moreover, for the sake of clarity, any quantity in 2D space of sublattices and four-dimensional space composed of valley and sublattice subspaces are labeled with *hat* and *check* signs, respectively.

Inside the parts of graphene covered by superconducting electrodes, an effective pair potential of the form $\check{\Delta} = \Delta \check{\mathbb{I}}$ is induced via proximity effect. We assume a phase difference ϕ between two superconductors with pairing functions $\Delta_{L,R} = \Delta_0 \exp(\pm i\phi/2)$, to drive the Josephson current. The coupling of electron and hole excitations ($\check{\Psi}_{e,h}$) inside these superconducting graphene regions is governed by the following Bogoliubov–de Gennes (BdG) equation,

$$\begin{pmatrix} \check{\mathcal{H}} - \mu & \check{\Delta} \\ \check{\Delta} & \mu - \check{\Theta}\check{\mathcal{H}}\check{\Theta}^{-1} \end{pmatrix} \begin{pmatrix} \check{\Psi}_e \\ \check{\Psi}_h \end{pmatrix} = \varepsilon \begin{pmatrix} \check{\Psi}_e \\ \check{\Psi}_h \end{pmatrix}, \qquad (2)$$

in which μ and ε indicate the chemical potential and the energy of the Bogoliubov quasiparticles, respectively. The time-reversed Hamiltonian corresponding to the hole-type excitations follows $\check{\Theta}\check{\mathcal{H}}(\mathbf{A}, \mathbf{A}_S)\check{\Theta}^{-1} = \check{\mathcal{H}}(-\mathbf{A}, \mathbf{A}_S)$, since under the act of time-reversal operator $\check{\Theta}$ the real magnetic fields change sign while the strain-induced gauge fields remain the same.

A. Constructing a semiclassical framework

In what follows we will construct a semiclassical picture for the propagation of massless Dirac particles at the presence of a general Abelian gauge potential $\mathcal{A}$ with contributions from both real magnetic field and geometric deformations. The starting point is to write the massless Dirac equation in the squared form,

$$v_F^2 [\hat{\boldsymbol{\sigma}} \cdot (\mathbf{p} + e\mathcal{A})]^2 \hat{\Psi} = E^2 \hat{\Psi}. \quad (3)$$

Assuming the gauge potentials are weak enough, we only keep the linear terms in $\mathcal{A}$ and corresponding gauge field $\mathcal{B} = \mathbf{z} \cdot (\nabla \times \mathcal{A})$ which results in

$$v_F^2 (\mathbf{p}^2 + 2e\mathcal{A} \cdot \mathbf{p} + \hbar e\mathcal{B}\hat{\sigma}_z)\hat{\Psi} = E^2 \hat{\Psi}. \quad (4)$$

The main step towards the semiclassical framework can be passed by considering the wavefunction as $\hat{\Psi}(\mathbf{r}) = e^{i\mathbf{k}\cdot\mathbf{r}}\hat{\psi}(\mathbf{r})$ composed of a plane-wave corresponding to the energy $E = \hbar v_F|\mathbf{k}|$ and a slowly varying envelope function $\hat{\psi}(\mathbf{r})$. Then we can ignore the second-order spatial derivative of $\hat{\psi}$ as well as the term proportional to $\mathcal{A} \cdot \nabla\hat{\psi}$ provided by two legitimate assumptions $|\nabla^2\hat{\psi}| \ll |\mathbf{k} \cdot \nabla\hat{\psi}|$ and $|e\mathcal{A}| \ll \hbar k$ when the energy E with respect to the Dirac point is high enough.[1] As a result we arrive in the following first-order equation of motion for the envelope function $\hat{\psi}(\mathbf{r})$,

$$(-2i\hbar^2\mathbf{k} \cdot \nabla + 2\hbar e\mathbf{k} \cdot \mathcal{A} + \hbar e\mathcal{B}\hat{\sigma}_z)\hat{\psi} = 0, \quad (5)$$

corresponding to the semiclassical trajectories determined by the direction of the wave-vector $\mathbf{n} = \mathbf{k}/k_F$ (throughout the paper only excitations at the vicinity of the Fermi level are considered).

It must be mentioned that under our assumption the trajectories are straight lines and the gauge fields are too weak to bend them. More precisely, the cyclotron radius $R_{\text{cyc}} \sim \hbar k_F/e\mathcal{B}$ over which the bending of a trajectory take place is much larger than length L and width W of the normal graphene region. In other words, we are limited to the cases in which $L, W \ll R_{\text{cyc}}$ provided by large Fermi wave vector or highly doped graphene. Figure 1(b) shows a few examples of classical trajectories starting from one SG interface and ending at another. It is clear that the trajectories are mirror reflected at the edges of the graphene sheet along the x direction where hard-wall boundary conditions must be satisfied. The trajectories can be fully determined by their initial position at the interface denoted by y_0 and the angle θ. Then each trajectory can be parametrized with a single parameter ℓ indicating the distance from the initial point along the trajectory. This leads to the following equation:

$$\partial_\ell \hat{\psi} = -\frac{ie}{\hbar}\left(\mathbf{n} \cdot \mathcal{A} + \frac{\mathcal{B}}{2k_F}\hat{\sigma}_z\right)\hat{\psi}, \quad (6)$$

which has the form of an evolution equation and provides a cornerstone for our semiclassical description of the Dirac equation at the presence of gauge fields.

Considering any trajectory $\mathcal{C}$, the above semiclassical equation can be (formally) integrated as $\hat{\psi}_{\mathcal{C}} = \exp[-i(\chi +$

$\chi'\hat{\sigma}_z)]\hat{\psi}_0$, with two gauge-induced phase factors,

$$\chi = \frac{\pi}{\Phi_0}\int_{\mathcal{C}} d\ell\, \mathbf{n} \cdot \mathcal{A}, \quad \chi' = \frac{\pi}{2k_F\Phi_0}\int_{\mathcal{C}} d\ell\, \mathcal{B}, \quad (7)$$

where $\Phi_0 = \pi\hbar/e$ is the superconducting magnetic-flux quantum. While the first phase χ is responsible for the conventional AB effect, the second one χ' is quite different and acts as a respective phase between the components of the spinor $\hat{\psi}$ rather than being an overall phase. In particular, Stokes' theorem guarantees that for a closed path, χ depends on the area enclosed by the closed trajectory $\mathcal{C}$ and more precisely the flux, however, χ' is a function of circumference. Another point that must be mentioned is that the AB phase χ for the closed paths and χ' for any trajectory (open or closed) are clearly gauge invariant, as expected. Considering a constant gauge field $\mathcal{B}_z$ and choosing a Landau gauge $\mathcal{A} = -\mathcal{B}_z y\, \mathbf{x}$, for a given trajectory determined by y_0 and θ, the two phase factors obey the following relations:

$$\chi = \frac{\pi S_{y_0,\theta}}{LW}\frac{\Phi_{\mathcal{B}}}{\Phi_0}, \quad \chi' = \frac{\pi}{2k_F W \cos\theta}\frac{\Phi_{\mathcal{B}}}{\Phi_0}. \quad (8)$$

Here, $\Phi_{\mathcal{B}} = LW\mathcal{B}$ is the gauge flux passing through the nonsuperconducting graphene region, and $S_{y_0,\theta}$ indicates the area enclosed between the trajectory and the lower parts of the normal region boundaries. The exact form of the area will be shown in the Appendix with details of the calculations. It will be very useful for the discussion in the next section if we rewrite the condition for having straight trajectories versus the scaled flux $\Phi_{\mathcal{B}}/\Phi_0$. One can simply check that the large cyclotron radius is equivalent to $\pi\Phi_{\mathcal{B}}/\Phi_0 \ll \min(k_F L, k_F W)$ where both $k_F L$ and $k_F W$ are very large to guarantee the validity of the semiclassical picture. Therefore, while for the angles $\theta \to \pm\pi/2$ the phase χ' could be very large, for the normal incidences ($\theta \ll 1$) which can give the dominant contribution in the current, χ' cannot be exceedingly large and is at most on the order of 1. Subsequently, we would not expect oscillatory behavior originating from χ' and as it will be clear soon only a conventional AB phase χ can give rise to the magnetic oscillations known as the Fraunhofer pattern of the critical current.

B. Bound-state energies and the supercurrent

Now using the semiclassical framework developed above and the BdG equations, we can find the bound-states energies ($|\varepsilon| < \Delta_0$) for any trajectory sandwiched between the interfaces. The formation of bound state can be usually understood as the result of successive Andreev reflections at the two interfaces [51]. Such Andreev bound states (ABSs) are current carrying and therefore responsible for the Josephson current in the short junction limit where the length is smaller than the superconducting coherence length ($L \ll \xi$). For the sake of clarity, we should mention that here we have only a so-called retro Andreev reflection because of a high Fermi level ($\varepsilon \ll \mu$) [24]. This is consistent with the fact that we are working at the level of the semiclassical picture where the Fermi wavelength λ_F is the smallest length scale. Then the electron and hole components of current carrying ABSs will propagate on the same trajectory. Subsequently, all dynamical phases accumulated during the propagation as well as those

---

[1]We should note that the energy must not be so high that trigonal warping effects come into play.

originating from the normal reflections at the edges cancel out between the electron and hole which go back and forth along the trajectory.

In order to find the ABS energies, we invoke Eq. (6) to see how electron and hole excitations evolve between the two interfaces at the presence of gauge fields. From the aforementioned properties of the magnetic and strain-induced gauge fields, we can write the total gauge potentials for electron and hole excitations from different valleys in the following form:

$$\mathcal{A}_{e,K} = \mathbf{A} + \mathbf{A}_S, \quad \mathcal{A}_{e,K'} = \mathbf{A} - \mathbf{A}_S,$$
$$\mathcal{A}_{h,K'} = -\mathbf{A} + \mathbf{A}_S, \quad \mathcal{A}_{h,K} = -\mathbf{A} - \mathbf{A}_S. \quad (9)$$

Subsequently, one can consider a similar structure for the phase factors χ and χ' decomposed to $\chi_{B,S}$ and $\chi'_{B,S}$ where subscripts B and S denote magnetic field and strain-induced gauge effects, respectively. Considering electrons and holes from valleys K and K', respectively, the corresponding spinors at the two interfaces are connected as below,

$$\hat{\psi}_{e,K}|_R = e^{-i(\chi_B + \chi_S) - i(\chi'_B + \chi'_S)\hat{\sigma}_z} \hat{\psi}_{e,K}|_L, \quad (10)$$

$$\hat{\psi}_{h,K'}|_R = e^{-i(-\chi_B + \chi_S) - i(-\chi'_B + \chi'_S)\hat{\sigma}_z} \hat{\psi}_{h,K'}|_L. \quad (11)$$

On the other hand, the superconducting correlations at the interfaces lead to electron-hole conversions governed by the following boundary condition [25,30]:

$$\hat{\psi}_{h,K'} = e^{\pm i(\frac{\phi}{2} + \beta\hat{\sigma}_x)}\hat{\psi}_{e,K}, \quad \beta = \arccos\left(\frac{\varepsilon}{\Delta_0}\right), \quad (12)$$

at left and right interfaces, respectively. Putting Eqs. (10)–(12) together, one can easily see that the formation of a bound state inside a normal graphene region is guaranteed when

$$\text{Det } \left[e^{i(\phi/2 + \beta\hat{\sigma}_x)} e^{-i(\chi_B + \chi_S) - i(\chi'_B + \chi'_S)\hat{\sigma}_z} \right.$$
$$\left. - e^{-i(-\chi_B + \chi_S) - i(-\chi'_B + \chi'_S)\hat{\sigma}_z} e^{-i(\phi/2 + \beta\hat{\sigma}_x)} \right] = 0. \quad (13)$$

This results in the following relation for the ABS energies:

$$\frac{\varepsilon}{\Delta_0} = \sqrt{\frac{\cos^2\left(\frac{\phi}{2} - \chi_B\right) - \sin^2 \chi'_S}{\cos^2 \chi'_B - \sin^2 \chi'_S}}, \quad (14)$$

as functions of the phase difference ϕ, the AB phase χ_B due to the real magnetic field, and the two anomalous phases χ'_B and χ'_S. Although the bound-state energies have been obtained by focusing on an electron (a hole) from the K point (K' point), one can easily check that considering the electron and hole excitations from the other valleys we will find exactly the same result. This is in agreement with the particle-hole symmetry present in superconducting heterostructures.

The most interesting property of the above relation is the fact that the strain-induced AB phase χ_S does not play any role in the ABS energies and the supercurrent, subsequently. One can interpret this result due to the cancellation of strain-induced AB phases accumulating in the electron and its time-reversal hole upon propagation along the trajectory. The magnetic AB phase χ_B acts as a shift in the phase difference ϕ between two S parts giving rise to an effective phase difference $\tilde{\phi}_B = \phi - 2\chi_B$ from which the magnetic oscillations and the famous Fraunhofer pattern originate [18,22,23]. Nevertheless, the two anomalous phases mostly impose the

limitation

$$\sin^2 \chi'_S \leqslant \cos^2(\tilde{\phi}_B/2) \leqslant \cos^2 \chi'_B, \quad (15)$$

on the range of effective phase difference $\tilde{\phi}$ in which bound states can be formed. A simple physical interpretation for the above relation can be provided if we notice that both $\chi'_{B,S}$ cause the Dirac spinors to rotate in the xy plane as given by Eqs. (10) and (11). Therefore, in order to have bound states, the rotation of electron and hole pseudospins during their propagation between two superconductors must be compensated. Interestingly it happens that the compensation is not possible for all effective phase differences ($\tilde{\phi}$), which subsequently gives rise to the limitation for having an ABS.

It is clear that for any trajectory $\mathcal{C}$ labeled by y_0 and θ, we will get a different bound state which can be denoted by $\varepsilon_{y_0,\theta}(\phi)$ and given by Eq. (14). In fact, under the semiclassical framework, there exists a continuous spectrum of ABS energies depending on the vertical intercept and the slope of the trajectories. Henceforth, the contribution of each bound state in the supercurrent can be obtained from the following relation for the Josephson current density [29,51]:

$$\delta I(y_0, \theta) = -\frac{4e}{\hbar} \frac{d\varepsilon_{y_0,\theta}(\phi)}{d\phi} \tanh\left[\frac{\varepsilon_{y_0,\theta}(\phi)}{2k_B T}\right], \quad (16)$$

at a temperature T ($T < T_c$). The total Josephson current can be obtained by summing over all trajectories as below,

$$I = \frac{k_F}{2\pi} \int_{-\pi/2}^{\pi/2} d\theta \cos\theta \int_0^W dy_0 \, \delta I(y_0, \theta). \quad (17)$$

In the following section, using Eqs. (8) and (14)–(17), we will study the effects of gauge fluxes originating from real magnetic fields and/or strains on the Josephson current in the SGS junctions.

III. RESULTS AND DISCUSSION

In this part, the results of the pseudomagnetic field effects induced by the strain on the variation of critical current as well as Josephson vortices and Fraunhofer pattern at the presence of a finite real magnetic field will be presented. It worth reminding that in order to validate the approximation of straight trajectories we are limited to large doping provided by $k_F L, k_F W \gg \pi \Phi_\mathcal{B}/\Phi_0$ as explained before ($\mathcal{B}$ stands for both real and pseudomagnetic fields). Since throughout the paper we will consider magnetic and pseudomagnetic fluxes in the range of $\Phi_\mathcal{B}/\Phi_0 \lesssim 10$, assuming $k_F L, k_F W \gtrsim 100$, our semiclassical approximation is well justified in all of the presented results.

A. Supercurrent enhancement by gauge fields

We first examine the effect of mere gauge fields induced by an arc-shape strain on the Josephson current. It is clear that here only the phase χ'_S or the corresponding flux $\Phi_S = LWB_s$ can affect the bound-state energies and the supercurrent, subsequently. The numerically obtained current-phase relation (CPR) for an SGS junction in the presence of a uniform gauge field is shown in Fig. 2 for different values of Φ_S/Φ_0. It shows that there is a range for superconducting phase differences ϕ in which the Josephson current is almost suppressed. In
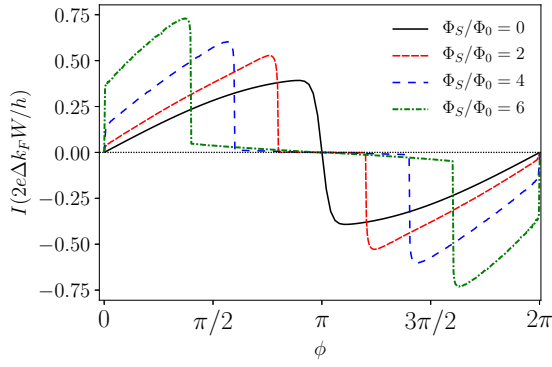
FIG. 2. Current-phase relation for the SGS junction under a uniform strain-induced gauge field of various strengths given by Φ_S/Φ_0. Increasing the applied gauge field leads to larger range of phase differences in which the Josephson current is suppressed. Simultaneously, the maximum values of the Josephson current increases monotonically with the gauge field. The geometric aspect ratio of junction is $W/L = 1$ and the temperature is considered to be $T = 0.05T_c$.

Sec. II B we noticed that the range of phase differences over which a bound state can exist is constrained due to the rotation of pseudospin caused by anomalous phases χ'. This results in a constraint on the range of ϕ's with finite Josephson current which can be approximately obtained from Eqs. (8) and (15) as

$$\pi - \frac{\pi}{2k_F W}\frac{\Phi_S}{\Phi_0} < \phi < \pi + \frac{\pi}{2k_F W}\frac{\Phi_S}{\Phi_0}, \qquad (18)$$

by considering only the normally incident trajectories ($\theta = 0$) which have the dominant contribution in the supercurrent. As a consequence of the confined range of ϕ's to have ABSs, by increasing Φ_S/Φ_0 the bound-state energies vary sharply with the phase difference and therefore the Josephson current can reach higher values as can be seen in Fig. 2. Then it follows that the critical current must be raised by increasing the strength of strain and corresponding gauge field. This is in contrast to the Fraunhofer-type behavior induced by real magnetic fields as shown in Fig. 3 for various aspect ratios of the junction and at two different temperatures. Interestingly, the effect of the gauge field is much stronger for a longer junction with smaller values of W/L as can be understood from the dependence of the gauge-induced anomalous phase χ' on the length following from Eq. (7).

B. Josephson vortices and Fraunhofer patterns

In this part, we would like to investigate the supercurrent density profiles in the presence of magnetic and pseudo-magnetic fields. As mentioned in the Introduction, when the normal region of an SNS junction is subjected to a uniform magnetic field, the supercurrent profile is strongly modulated due to the quantum interferences which lead to the vortexlike circular flow patterns. In the semiclassical picture, the local current density at each point can be obtained by summing over the contributions of all trajectories passing through that point or equivalently by mere integration over θ. Figure 4 shows the supercurrent profile of a conventional SNS junction and SGS junctions in the presence of a gauge field of various strengths
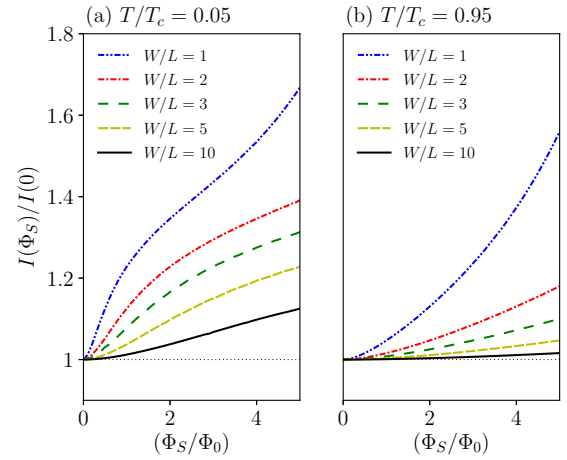

FIG. 3. Variation of critical current with the strength of strain-induced gauge field for some aspect ratios of the junction. Panels (a) and (b) correspond to the temperatures $T = 0.05T_c$ and $T = 0.05T_c$. In general, the critical current monotonically increases with the gauge field, however the amplitude of variations is larger for smaller geometric aspect ratios.

$\Phi_S/\Phi_0 = 0, 1, 2$, all subjected to a constant magnetic field flux $\Phi_B/\Phi_0 = 4$ and a phase difference $\phi = \pi/4$ between two S electrodes. In all cases series of vortices and antivortices are seen which are mainly located at the middle of the junction. Furthermore, we see that compared to an SNS junction, the SGS case has a more profound and localized vortex structure. Intriguingly, when the strain is imposed to the graphene, the local Josephson current is further localized by increasing the strength of the gauge field.

It is very instructive to discuss how vortex patterns are formed in Josephson current density in a generic SNS system, before providing a detailed discussion about the SGS junction and the role of strain-induced gauge fields. To this end, let us first examine the current density over the vertical line exactly at the middle of the junction ($x = L/2$). One can easily see that the current flows in the horizontal direction there. The reason comes from the mirror symmetry between the trajectories with opposite angles $\pm\theta$ passing from the line $x = L/2$, which subsequently results in the same AB phases and differential current amplitudes $\delta I(\theta) = \delta I(-\theta)$ (one should remember that the AB phase χ is proportional to the area underneath the trajectory). In addition, all straight trajectories crossing the point ($x = L/2, y$) enclose the same area below themselves and as a result, their contributions to the local current add up coherently. Then moving along the vertical direction, the AB phase χ_B linearly increases with y for most of the trajectories. Therefore one can conclude that the bound-state energies and the Josephson current density vary almost periodically along the y direction according to Eqs. (14) and (16). Deviation from perfect periodic variations becomes visible close to the horizontal boundaries of the junction where a substantial part of the trajectories is reflected once or more at the edges. In contrast to the straight paths, the zigzag ones passing from a certain point in the middle of the junction can have different areas below them which give rise to different AB phases as well. So we would expect a weak
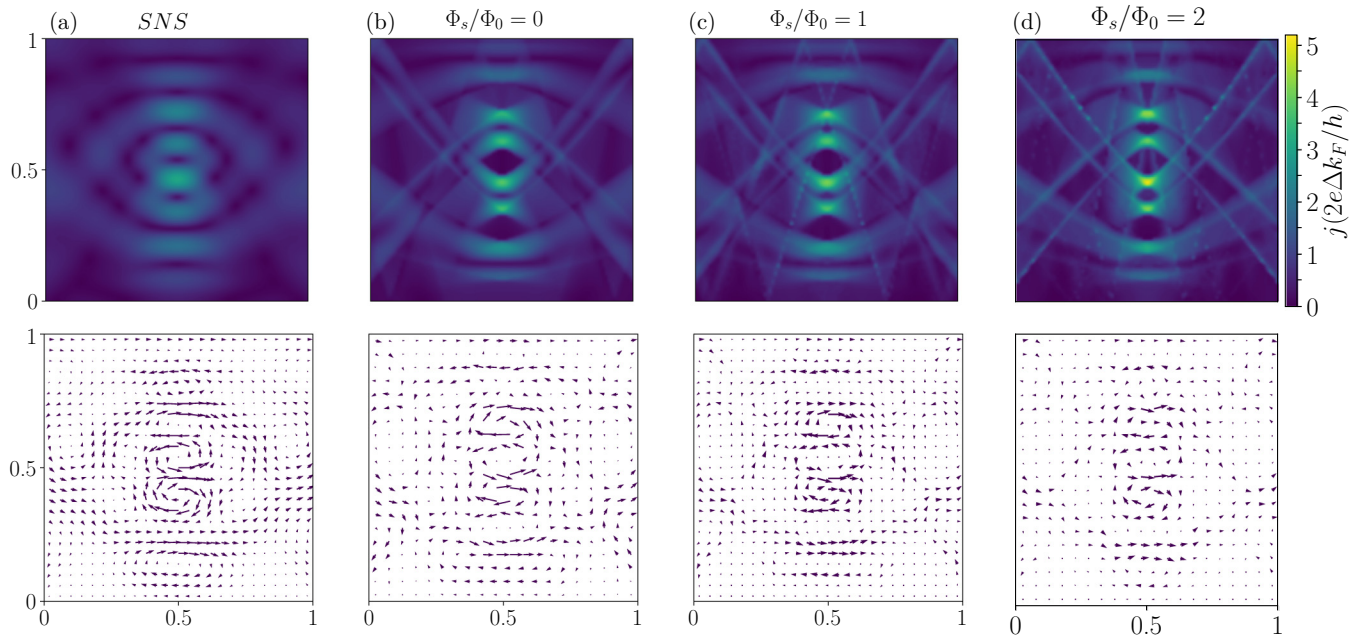
FIG. 4. Formation of Josephson vortices at the presence of magnetic flux $\Phi_B/\Phi_0 = 4$ in (a) an SNS junction and (b)–(d) SGS junctions subjected to different values of strain-induced gauge fields. Each column corresponds to the same situation with upper and lower panels indicating the intensity plot and the vector field of the local current density, respectively. While the generic form of the vortex pattern remains almost the same in all cases, the local current profile in SGS junctions has a more localized pattern. The localization is intensified at the presence and by increase of the gauge field. The parameters considered in all subplots are $W/L = 1$, $\phi = \pi/4$, and $T/T_c = 0.95$.

aperiodicity which can be moderate close to the horizontal edges as seen in Fig. 4(a). Away from the middle of the junction, $\delta I(\theta)$ will be no longer symmetric with respect to the angle because of the difference in the areas $S(y_0, \pm\theta)$. Therefore, the local current at points $x \neq L/2$ after integration over θ can have a vertical component which qualitatively explains the appearance of the circular flow pattern around certain points mostly located at $x = L/2$. Moreover, besides the major line of the vortex-antivortex series, very weak vortex flows can be found far from the middle of the junction and close to the SG interfaces.

When we turn to the graphene-based Josephson junctions, at the presence of a real magnetic field, the anomalous phase χ'_B will come into play besides the AB phase. We have already seen in previous parts that the anomalous phases lead to the pseudospin rotation which subsequently puts some constraints on the range of parameters over which ABS can be formed. So for any constant phase difference ϕ, due to the constraint given by Eq. (15) some trajectories could not give rise to ABS in contrast to the SNS junction. Moreover, on the same ground as we discussed, the underlying physics of Josephson current enhancement by the gauge fields, the trajectories hosting an ABS give rise to larger Josephson current. Putting it all together, we can understand why the profile of the local supercurrent density is more localized and has larger peaks in graphene-based Josephson junctions as seen in Fig. 4(b) compared to an SNS junction. On the same ground, when strain is applied to graphene, the corresponding anomalous phase χ'_S leads to further localization of the local current flow patterns. In fact as it is seen from Figs. 4(c) and 4(d) the interference pattern is not drastically influenced by the pseudomagnetic fields as long as the their strength is not strong compared to

the real magnetic field. So when $\Phi_S \lesssim \Phi_B$, the major effect of pseudomagnetic fields is that the spatial variations become increasingly sharper at the presence of a finite Φ_S. This is again along with the fact that strain-induced gauge fields have not any AB-type effect which can result in further modulation of the supercurrent.

When the gauge fields originating from the strain are strong enough in comparison to the applied magnetic field, another interesting phenomenon shows up. This new effect is the appearance of a finite region where the current is almost suppressed due to the gauge fields, as can be clearly seen in Fig. 5(d) where a large pseudomagnetic flux $\Phi_S/\Phi_0 = 5$ is imposed to the junction. Such behavior is essentially different from the main trend in Figs. 5(a)–5(c) corresponding to $\Phi_S/\Phi_B = 0, 1, 3$ in which the supercurrent only becomes slightly squeezed by the pseudomagnetic field in accordance with the above discussion. A big difference of the new region with conventional vortex cores is that it has a much sharper boundary with the region of finite supercurrent as can be seen from Fig. 5(d). Interestingly the halo region of supercurrent suppression induced by a large pseudomagnetic field is placed on top of the junction which has the largest supercurrent when $\Phi_S = 0$. The origin of new vortex cores is indeed nothing but the constraint (15) in which by increasing the anomalous phase χ'_S from 0 to $\pi/2$ the range of effective phase differences $\tilde{\phi}_B = \phi - 2\chi_B$ with contribution in the current decreases. Therefore, for a constant phase difference ϕ, the AB phase χ_B or equivalently the trajectories with nonvanishing current will be constrained. To better illustrate this effect let us consider the normally incident trajectories ($\theta = 0$) for which the AB phase is simply $\chi_B = \pi(\Phi_B/\Phi_0)(y/W)$. Then we can rewrite the constraint due to the strain-induced anomalous
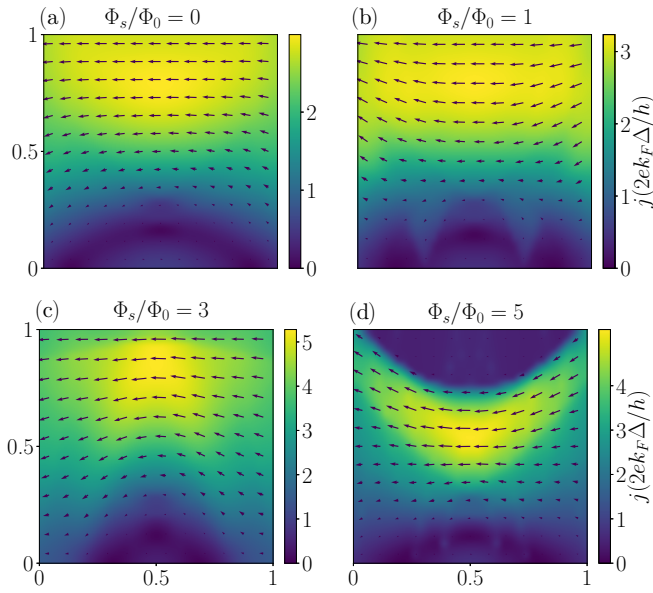
FIG. 5. Evolution of local current density profile with pseudo-magnetic field in the presence of a constant magnetic flux $\Phi_B/\Phi_0 = 0.5$. While the trend from (a) to (c) indicates that only local current becomes more localized and the maximum values increase, the behavior in the presence of large gauge field ($\Phi_S/\Phi_0 = 5$) is drastically different. In the last situation a big halo appears on the top of the junction where the supercurrent is almost diminished. The halo region has sharp boundaries with its surroundings in contrast to the conventional vortex cores (like the one on the lower edge) where the current density varies smoothly with the distance from the vortex center. The other parameters used here are the same as those in Fig. 4.
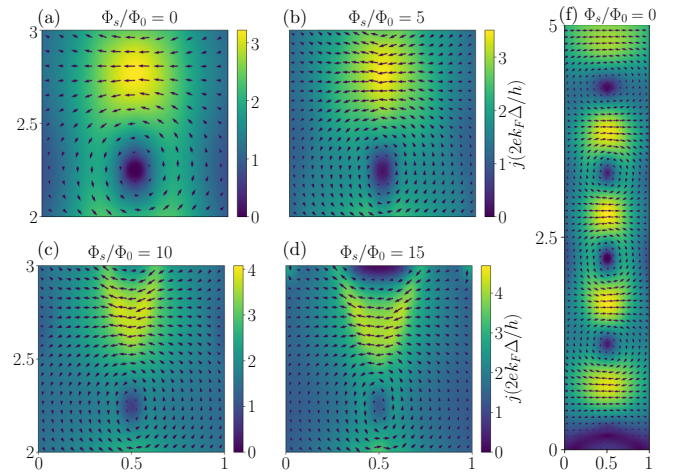

FIG. 6. (a)–(d) Local current density profile inside the middle portion of a wide junction with $W/L = 5$ at the presence of a constant total magnetic flux $\Phi_B/\Phi_0 = 2.5$ passing through the junction and different pseudomagnetic fluxes $\Phi_S/\Phi_0 = 0, 5, 10, 15$, respectively. The portion is extended from $y/L = 2$ to $y/L = 3$ along vertical direction while it fills the whole length of the junction ($0 < x/L < 1$). Compared to Fig. 5 the current profile is more localized along the central vertical line but it shows qualitatively similar behavior by increasing Φ_S as before. It should be noted that the flux passing through the portion is 1/5 of the total flux which makes the comparison with those in Fig. 5 reasonable. (f) Shows the local current throughout the junction when $\Phi_S/\Phi_0 = 0$ in correspondence to panel (a). It clearly shows an almost periodic variation of the current along vertical direction. All other parameters used here are the same as those in Fig. 5.

phase as below:

$$\left| \cos\left(\frac{\phi}{2} - \pi \frac{\Phi_B}{\Phi_0} \frac{y}{W} \right) \right| \geqslant \sin\left(\frac{\pi}{2k_F W} \frac{\Phi_S}{\Phi_0} \right). \qquad (19)$$

Invoking the parameters used in Fig. 5(d), one can easily see that for $y/W > 3/4$ the above condition is not satisfied. Therefore all trajectories with $\theta = 0$ and $y_0 > 3/4$ do not carry a supercurrent which suggests by itself that there must be a region of strong supercurrent suppression around the upper edge of the junction. By more detailed analysis of the other trajectories one can obtain the precise boundary of the halo region with the surrounding in Fig. 5(d).

So far we have discussed the Josephson vortex formation in the special geometry of a square-shape junction ($W = L$) in which the reflected trajectories from the two graphene edges also have a substantial contribution to the local currents. However, it should be mentioned that we are still in the limit of $W, L \ll R_{\text{cyc}}$, so we can ignore any deflection of the trajectories and particularly there will be no skipping orbits. In fact, skipping orbits play a crucial role when $L > R_{\text{cyc}}$ which is the opposite limit of what we are exploring here [49,50]. On the other hand, for wide junctions ($W \gg L$), while keeping the length comparatively smaller than the cyclotron radius, we can still rely on our semiclassical description and furthermore the reflected trajectories have a very minor role in these cases. As we see from Fig. 6, where the local Josephson current density at the middle of a wide junction with $W/L = 5$ is plotted for various strengths of strain-induced gauge fluxes,

almost all the aforementioned features of Josephson vortices influenced by the pseudomagnetic fields are detained. In fact, upon increasing Φ_S we see that the local current density becomes localized showing enhanced maximum value, besides the appearance of new vortex cores at larger strain-induced fluxes. Moreover, comparing the results of Figs. 5 and 6, we immediately realize that in wide junctions the current profile and vortices are much more localized along the line $x = L/2$ at the middle of the junction, yet in the square-shape case ($W \sim L$) the reflected trajectories lead to broadened current density profiles as described before.

At the end of this part, we examine evolution of the Fraunhofer patterns with the pseudomagnetic field as depicted in Fig. 7. In the absence of the gauge field ($\Phi_S = 0$), the conventional magnetic oscillations of the critical current are retained. Particularly at the limit of wide junctions $W/L \gg 1$, the period of oscillations $\delta\Phi_B$ is Φ_0 while for narrower junctions with $W/L \lesssim 1$, it switches to $2\Phi_0$ in agreement with previous investigations in SGS and SNS systems [22,47]. When a constant pseudomagnetic or gauge field is present, the overall behavior of the Fraunhofer pattern remains almost the same as when it is absent except for an increase in the maximum current at $\Phi_B = 0$. This result again originates from the fact that gauge fields do not cause any AB-type oscillation or modulation of the supercurrent. Returning back to the discussion over the supercurrent density profiles, when the magnetic field was strong enough to modulate the current and induce
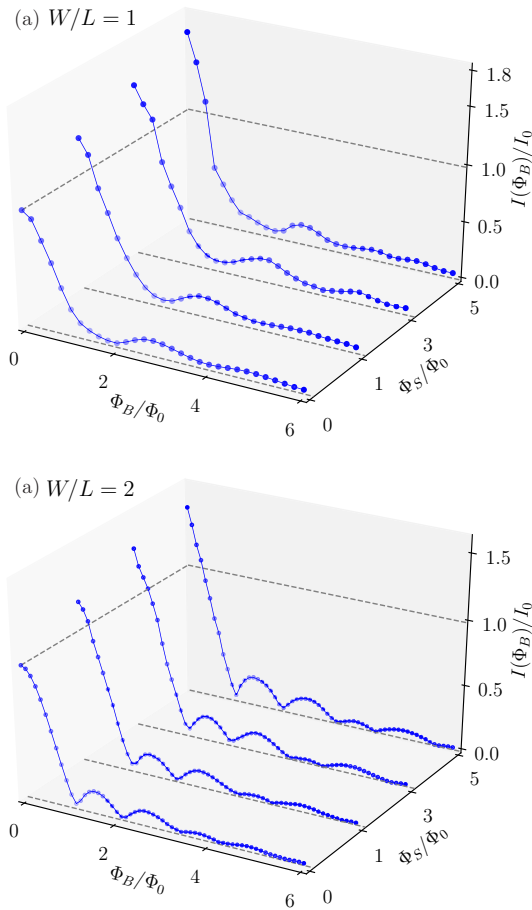
FIG. 7. Magnetic oscillations of the critical Josephson current known as Fraunhofer pattern when the graphene junction is subjected to the pseudomagnetic fields of different strengths $\Phi_S/\Phi_0 = 0, 1, 3, 5$. Panels (a) and (b) correspond to different width to length ratios of the junction $W/L = 1, 2$, respectively. While the maximum value of the critical current at $\Phi_B = 0$ increases monotonically with the pseudomagnetic field, its effect is less apparent at larger magnetic fluxes. By increasing the width of the junction, oscillations become more regular while aperiodic behavior appears when $W \lesssim L$.

couples of vortices inside the junction, the pseudomagnetic field leads to squeezed profiles with sharper peaks. So when we look at the whole critical current passing through the junction, these details are washed out by integration over the local current density, a fact that justifies why the Fraunhofer pattern is not strongly influenced by gauge fields. In other words, as it has been already seen in our other results in Sec. III A and Figs. 3 and 5, the effect of gauge fields is very strong either in the absence of real magnetic fields or when the real magnetic flux is small, namely $\Phi_B/\Phi_0 \lesssim 1$.

C. Discussion and experimental relevance

As mentioned in the Introduction, the emergence of gauge fields due to the strain is a result of its 2D nature as well as the Dirac character of the quasiparticles. While many theoretical and experimental investigations have been carried out to understand and exploit the strain-induced gauge fields for possible applications, only a few works focused on the

interference phenomena, especially the AB effect due to the gauge fields. Among them was an interesting proposal made by de Jaun *et al.* [12] to observe interference effects due to a local deformation in the electronic propagation encircling the strained region. Here we have focused on the graphene-based superconducting heterostructures and investigated the gauge field effects on the Josephson current, its density profile, and magnetic oscillation pattern. As it has been shown above, the critical Josephson current as well as the local supercurrent density are qualitatively influenced by the presence of strain-induced pseudomagnetic fields. It should be mentioned that the fact that ABSs are formed from time-reversal partners introduces a fundamental difference between the superconducting system we are studying and the AB interferometry scenario in Ref. [12]. Here the AB phases attributed to the gauge field do not enter in the supercurrent at all and only the anomalous phase factor χ'_S which corresponds to pseudospin rotation governs the underlying physics of our findings. Of particular importance is that in the SGS junction, the Josephson current is unexpectedly enhanced by strain-induced gauge fields.

All the predicted features can be possibly tested in future experiments provided by the validity of some assumptions in the current work. First of all, the excitations should keep their phase coherence while propagating throughout the junction. However this is not an elusive situation to current experimental devices and phase coherence lengths in SGS systems could be large enough compared to the junction size [42,43,45,52]. On the other hand, one may truly doubt the validity of our results at the presence of strong intervalley scatterings which can mix the electrons (or holes) from the two valleys. But nowadays very clean samples of suspended graphene can be manufactured with weak or moderate intervalley scatterings [53,54]. Therefore the overall experimental feasibility of our theoretical study is quite high even for the currently available setups.

IV. CONCLUSIONS

In this work, we have found anomalous quantum interference effects in graphene-based Josephson junctions subjected to the strain-induced pseudomagnetic fields besides real magnetic fields. As a key finding, it has been shown that the Josephson current is enhanced by applying an arc-shaped strain which gives rise to a constant pseudomagnetic or gauge field inside the graphene region sandwiched between superconductors. Such behavior is in complete contrast to the well-known Fraunhofer pattern of the critical current with an oscillatory decaying dependence on the magnetic flux. The fundamental difference between real magnetic fields and strain-induced gauge fields regarding their symmetries under time reversal has been proven to be responsible for very different effects of magnetic and pseudomagnetic fluxes. We further have studied the combined effects of both types of fields simultaneously applied to the graphene Josephson junction. While the magnetic fields leads to the formation of Josephson vortices and the Fraunhofer pattern, the presence of gauge fields results in the squeezing of the local current density in circular flow patterns. Moreover, it has been revealed that stronger gauge fields compared to the magnetic fields can

affect the supercurrent flow pattern more crucially by forming large vortex cores with almost vanishing current in a finite region. So, our investigation has revealed unexpected features of the interference phenomena in graphene-based Josephson junction due to the strain-induced gauge fields which trigger further theoretical and experimental studies on the physics of gauge fields in graphene/superconductor hybrid structures.

APPENDIX: CALCULATION OF AREA ENCLOSED BY TRAJECTORIES

Here we calculate the Aharonov-Bohm phase of each trajectory and give the exact form of the corresponding area $S_{y_0,\theta}$. By choosing the Landau gauge as $\mathcal{A} = \mathcal{B}y\mathbf{x}$ it is clear that the line integral of gauge potential along the vertical NS interfaces as well as the lower edge of the graphene vanishes. So the contribution of the trajectory $\mathcal{C}$ in the line integral is the same as the corresponding closed loop and can be related to the area underneath $\mathcal{C}$ via Stokes' theorem,

$$\int_{\mathcal{C}} d\ell \mathbf{n} \cdot \mathcal{A} = \mathcal{B}S_{y_0,\theta}. \tag{A1}$$

Now in order to calculate $S_{y_0,\theta}$, for a given angle θ and offset y_0, we first determine the position and the number of reflection points of the trajectory at the two edges. For the sake of simplicity we divide the discussion to two parts for positive and negative angles. When $0 < \theta < \pi/2$ we have

$$N = \left(\frac{y_0 + L\tan\theta}{W} \right), \tag{A2}$$

$$x_n = (nW - y_0)\cot\theta, \quad 1 \leqslant n \leqslant N, \tag{A3}$$

respectively. Then by simple geometry we can obtain the area for three different cases of $N = 0$, an even N, and an odd N, follows, respectively:

$$S_{y_0,\theta} = Ly_0 + \frac{L^2}{2}\tan\theta, \tag{A4}$$

$$S_{y_0,\theta} = y_0\frac{x_1}{2} + W\frac{x_N}{2} + \frac{(L-x_N)^2}{2}\tan\theta, \tag{A5}$$

$$S_{y_0,\theta} = y_0\frac{x_1}{2} + W\left(L - \frac{x_N}{2}\right) - \frac{(L-x_N)^2}{2}\tan\theta. \tag{A6}$$

Similarly for negative angles $(-\pi/2 < \theta \leqslant 0)$ we can obtain the number of reflections and their x positions:

$$N = \left(\frac{W - y_0 + L|\tan\theta|}{W} \right), \tag{A7}$$

$$x_n = [(n-1)W + y_0]|\cot\theta|, \quad 1 \leqslant n \leqslant N. \tag{A8}$$

Subsequently, the area for $N = 0$, an even N, and an odd N when θ is negative angles can be obtained as

$$S_{y_0,\theta} = Ly_0 - \frac{L^2}{2}|\tan\theta|, \tag{A9}$$

$$S_{y_0,\theta} = (y_0 - W)\frac{x_1}{2} + W\frac{x_N}{2} + \frac{(L-x_N)^2}{2}|\tan\theta|, \tag{A10}$$

$$S_{y_0,\theta} = (y_0 - W)\frac{x_1}{2} + W\left(L - \frac{x_N}{2}\right) - \frac{(L-x_N)^2}{2}|\tan\theta|, \tag{A11}$$

respectively.

[1] A. H. Castro Neto, F. Guinea, N. M. R. Peres, K. S. Novoselov, and A. K. Geim, Rev. Mod. Phys. **81**, 109 (2009).

[2] K. S. Novoselov, V. I. Fal'ko, L. Colombo, P. R. Gellert, M. G. Schwab, and K. Kim, Nature (London) **490**, 192 (2012).

[3] J. González, F. Guinea, and M. A. H. Vozmediano, Phys. Rev. Lett. **69**, 172 (1992).

[4] H. Suzuura and T. Ando, Phys. Rev. B **65**, 235412 (2002).

[5] J. L. Mañes, Phys. Rev. B **76**, 045430 (2007).

[6] S. V. Morozov, K. S. Novoselov, M. I. Katsnelson, F. Schedin, L. A. Ponomarenko, D. Jiang, and A. K. Geim, Phys. Rev. Lett. **97**, 016801 (2006).

[7] A. F. Morpurgo and F. Guinea, Phys. Rev. Lett. **97**, 196804 (2006).

[8] M. A. Vozmediano, M. Katsnelson, and F. Guinea, Phys. Rep. **496**, 109 (2010).

[9] F. Guinea, A. K. Geim, M. I. Katsnelson, and K. S. Novoselov, Phys. Rev. B **81**, 035408 (2010).

[10] F. Guinea, M. Katsnelson, and A. Geim, Nat. Phys. **6**, 30 (2010).

[11] N. Levy, S. Burke, K. Meaker, M. Panlasigui, A. Zettl, F. Guinea, A. C. Neto, and M. Crommie, Science **329**, 544 (2010).

[12] F. De Juan, A. Cortijo, M. A. Vozmediano, and A. Cano, Nat. Phys. **7**, 810 (2011).

[13] A. Tonomura, N. Osakabe, T. Matsuda, T. Kawasaki, J. Endo, S. Yano, and H. Yamada, Phys. Rev. Lett. **56**, 792 (1986).

[14] M. Tinkham, *Introduction to Superconductivity* (Courier Corporation, North Chelmsford, 1996).

[15] R. Doll and M. Näbauer, Phys. Rev. Lett. **7**, 51 (1961).

[16] B. S. Deaver and W. M. Fairbank, Phys. Rev. Lett. **7**, 43 (1961).

[17] J. M. Rowell, Phys. Rev. Lett. **11**, 200 (1963).

[18] P. W. Anderson and J. M. Rowell, Phys. Rev. Lett. **10**, 230 (1963).

[19] R. C. Jaklevic, J. Lambe, A. H. Silver, and J. E. Mercereau, Phys. Rev. Lett. **12**, 159 (1964).

[20] J. Clarke and A. I. Braginski, *The SQUID Handbook: Applications of SQUIDs and SQUID Systems* (John Wiley & Sons, Weinheim, 2006).

[21] D. Roditchev, C. Brun, L. Serrier-Garcia, J. C. Cuevas, V. H. L. Bessa, M. V. Milošević, F. Debontridder, V. Stolyarov, and T. Cren, Nat. Phys. **11**, 332 (2015).

[22] U. Ledermann, A. L. Fauchère, and G. Blatter, Phys. Rev. B **59**, R9027(R) (1999).

[23] V. P. Ostroukh, B. Baxevanis, A. R. Akhmerov, and C. W. J. Beenakker, Phys. Rev. B **94**, 094514 (2016).

[24] C. W. J. Beenakker, Phys. Rev. Lett. **97**, 067007 (2006).

[25] M. Titov and C. W. J. Beenakker, Phys. Rev. B **74**, 041401 (2006).

[26] S. Bhattacharjee and K. Sengupta, Phys. Rev. Lett. **97**, 217001 (2006).

[27] A. G. Moghaddam and M. Zareyan, Appl. Phys. A **89**, 579 (2007).

[28] J. Linder, T. Yokoyama, D. Huertas-Hernando, and A. Sudbø, Phys. Rev. Lett. **100**, 187004 (2008).

[29] A. G. Moghaddam and M. Zareyan, Phys. Rev. B **78**, 115413 (2008).

[30] C. W. J. Beenakker, Rev. Mod. Phys. **80**, 1337 (2008).

[31] I. Hagymási, A. Kormányos, and J. Cserti, Phys. Rev. B **82**, 134516 (2010).

[32] B. Z. Rameshti, M. Zareyan, and A. G. Moghaddam, Phys. Rev. B **92**, 085403 (2015).

[33] H. B. Heersche, P. Jarillo-Herrero, J. B. Oostinga, L. M. Vandersypen, and A. F. Morpurgo, Nature (London) **446**, 56 (2007).

[34] X. Du, I. Skachko, and E. Y. Andrei, Phys. Rev. B **77**, 184507 (2008).

[35] C. Girit, V. Bouchiat, O. Naaman, Y. Zhang, M. F. Crommie, A. Zettl, and I. Siddiqi, Nano Lett. **9**, 198 (2009).

[36] C. Ojeda-Aristizabal, M. Ferrier, S. Guéron, and H. Bouchiat, Phys. Rev. B **79**, 165436 (2009).

[37] I. V. Borzenets, U. C. Coskun, S. J. Jones, and G. Finkelstein, Phys. Rev. Lett. **107**, 137005 (2011).

[38] G.-H. Lee, D. Jeong, J.-H. Choi, Y.-J. Doh, and H.-J. Lee, Phys. Rev. Lett. **107**, 146605 (2011).

[39] U. C. Coskun, M. Brenner, T. Hymel, V. Vakaryuk, A. Levchenko, and A. Bezryadin, Phys. Rev. Lett. **108**, 097003 (2012).

[40] N. Mizuno, B. Nielsen, and X. Du, Nat. Commun. **4**, 2716 (2013).

[41] J.-H. Choi, G.-H. Lee, S. Park, D. Jeong, J.-O. Lee, H.-S. Sim, Y.-J. Doh, and H.-J. Lee, Nat. Commun. **4**, 2525 (2013).

[42] V. E. Calado, S. Goswami, G. Nanda, M. Diez, A. R. Akhmerov, K. Watanabe, T. Taniguchi, T. M. Klapwijk, and L. M. K. Vandersypen, Nat. Nanotechnol. **10**, 761 (2015).

[43] M. B. Shalom, M. J. Zhu, V. I. Fal'ko, A. Mishchenko, A. V. Kretinin, K. S. Novoselov, C. R. Woods, K. Watanabe, T. Taniguchi, A. K. Geim, and J. R. Prance, Nat. Phys. **12**, 318 (2016).

[44] F. Deon, S. Šopić, and A. F. Morpurgo, Phys. Rev. Lett. **112**, 126803 (2014).

[45] M. T. Allen, O. Shtanko, I. C. Fulga, A. R. Akhmerov, K. Watanabe, T. Taniguchi, P. Jarillo-Herrero, L. S. Levitov, and A. Yacoby, Nat. Phys. **12**, 128 (2016).

[46] D. K. Efetov, L. Wang, C. Handschin, K. B. Efetov, J. Shuang, R. Cava, T. Taniguchi, K. Watanabe, J. Hone, C. R. Dean, and P. Kim, Nat. Phys. **12**, 328 (2016).

[47] P. Rakyta, A. Kormányos, and J. Cserti, Phys. Rev. B **93**, 224510 (2016).

[48] B. Uchoa and Y. Barlas, Phys. Rev. Lett. **111**, 046604 (2013).

[49] K. G. S. H. Gunawardana and B. Uchoa, Phys. Rev. B **91**, 241402 (2015).

[50] L. Covaci and F. M. Peeters, Phys. Rev. B **84**, 241401 (2011).

[51] C. W. J. Beenakker and H. van Houten, Phys. Rev. Lett. **66**, 3056 (1991).

[52] M. T. Allen, O. Shtanko, I. C. Fulga, J. I.-J. Wang, D. Nurgaliev, K. Watanabe, T. Taniguchi, A. R. Akhmerov, P. Jarillo-Herrero, L. S. Levitov, and A. Yacoby, Nano Lett. **17**, 7380 (2017).

[53] R. V. Gorbachev, J. C. W. Song, G. L. Yu, A. V. Kretinin, F. Withers, Y. Cao, A. Mishchenko, I. V. Grigorieva, K. S. Novoselov, L. S. Levitov, and A. K. Geim, Science **346**, 448 (2014).

[54] J. R. Schaibley, H. Yu, G. Clark, P. Rivera, J. S. Ross, K. L. Seyler, W. Yao, and X. Xu, Nat. Rev. Mater. **1**, 16055 (2016).